JOURNAL OF MAGNETIC RESONANCE **135,** 156–164 (1998)
ARTICLE NO. MN981537

Relaxation Time Mapping of Short T_2^* Nuclei with Single-Point Imaging (SPI) Methods

Steven D. Beyea, Bruce J. Balcom,[1] Pablo J. Prado, Albert R. Cross, Christopher B. Kennedy, Robin L. Armstrong, and Theodore W. Bremner*

*Department of Physics, MRI Centre; and *Department of Civil Engineering, P.O. Box 4400, University of New Brunswick, Fredericton, New Brunswick, E3B 5A3, Canada*

Received January 21, 1998; revised June 15, 1998

New techniques for quantitative mapping of T_1, T_2, and T_2^* are proposed, based on the *s*ingle-*p*oint *i*maging (SPI) method, for materials with short nuclear magnetic resonance relaxation times which cannot be imaged with traditional methods. Relaxation times extracted from two-dimensional images of uniform doped agarose phantoms ($T_2^* \approx 60$–210 μs) as well as hardened mortar ($T_2^* \approx 220$ μs) and polymers ($T_2^* \approx 20$–100 μs), using these techniques, agreed with bulk measurements. The method was then applied to a partially dried cylindrical concrete sample ($T_2^* \approx 115$ μs).

INTRODUCTION

The recent development of broad-line imaging techniques (*1–3*) has led to a renewed interest in MRI of industrially relevant materials ranging from polymers and ceramics (*4, 5*) to porous rocks (*6, 7*) and building materials (*8–10*). One of the most promising of these solid state techniques is the *s*ingle-*p*oint (or constant time) *i*maging (SPI) technique, originally proposed by Emid and Creyghton (*11*). A number of variations have been proposed in the literature (*12–15*), including our own development, SPRITE (*s*ingle-*p*oint *r*amped *i*maging with T_1 *e*nhancement) (*15*). We have demonstrated the usefulness of SPI/SPRITE for imaging cement (*8*) and concrete (*16, 17*) materials, which have short transverse and longitudinal relaxation times, as well as for space resolved calorimetry and pore size distributions (*18, 19*).

A large body of work exists in the literature concerning the interpretation of bulk NMR relaxation times in materials (*20–22*). For inhomogeneous materials, however, measurements in bulk are not sufficient because the NMR relaxation times will vary spatially (*23–26*). The oscillating gradient recalled echo method has been used for relaxation time mapping of porous water saturated materials; however, technical limitations on the oscillation period ($TE_{\min} \approx 200$ μs) limit the shortest measurable relaxation time (*27, 28*). The *stray-field imaging* (STRAFI) technique has been employed to map very short spin–spin relaxation times (*29, 30*); however, the observed decay is a complex mixture of T_2 (spin–spin relaxation) and $T_{1\rho}$ (spin–lattice relaxation in the rotating frame) time constants, which complicates the interpretation (*31, 32*). SPI/SPRITE techniques span the range of relaxation times accessible via the STRAFI and oscillating gradient echo techniques, without the need for specialized equipment or hardware modifications. SPI techniques have been used to image samples which range from long T_2 animal tissue, with resolution of $5 \times 5 \times 50$ μm^3 (*33*), to short T_2 polymers (*4*). The principal restrictions on both the resolution and sensitivity of SPI techniques are the RF probe deadtime and maximum gradient strength, as well as molecular diffusion (*33*).

In the present study, we wish to introduce a systematic study of four new relaxation time mapping methods to quantitatively map T_1, T_2, and T_2^*, based on the SPI/SPRITE technique.

EXPERIMENTAL DETAILS

Imaging methods were implemented on a Nalorac (Martinez, CA) 2.35 Tesla 32-cm i.d. horizontal bore superconducting magnet. The gradient sets used were a water-cooled 20-cm i.d. self-shielded gradient set (maximum gradient 10 G/cm), and a 7.5-cm i.d. water-cooled gradient set (maximum gradient 100 G/cm). Both were driven by Techron (Elkhart, IN) 7780 amplifiers. Experiments were performed with a Tecmag (Houston, TX) Libra S-16 console at ambient temperature, using homebuilt bird-cage coils, driven by a 2-kW AMT (Brea, CA) 3445 RF amplifier. All parameter values and standard errors obtained from the fit data were determined using the Levenberg–Marquardt algorithm (*34*).

The validation images shown are of three different phantoms, chosen to demonstrate the range of relaxation times which can be mapped using these methods. The phantoms themselves have uniform relaxation times, so as to be able to compare the values obtained from the mapping to the individual bulk values. Two of the phantoms were 12-mm diameter Mn(II)-doped 1% agarose gels (Sigma Chemical), with bulk T_2's of 210.4 ± 0.4 μs and 65 ± 2 μs, and T_1's of 2.58 ± 0.01

[1] To whom correspondence should be addressed.

1090-7807/98 $25.00

ms and 0.70 ± 0.01 ms, respectively. T_2^* relaxation times were equal to that of the T_2, due to the fact that line broadening due to field inhomogeneities was insignificant compared to the spin–spin relaxation. The third phantom was a 10 mm × 10 mm × 25 mm white Portland cement mortar sample.[2] Blinc *et al.* (*22*) have shown that T_1 in hydrated cementious materials can be described by a stretched exponential, which corresponds to the fractal geometry of the pore structure. Bulk values for the mortar, fit to a stretched exponential, were $\tilde{T}_1 = 1.28 \pm 0.02$ ms ($\alpha = 0.69 \pm 0.05$). The T_2^* of the mortar was best fit to a single exponential with a decay constant of 218 ± 1 μs.

BASIC SPI/SPRITE METHODS

We will first consider general properties of the SPI method. The signal amplitude in the longitudinal steady state, *S*, following a brief (broadband, non-slice selective) RF pulse, α, from any point in the image is given by Eq. [1],

$$S = \rho \exp\left(-\frac{t_p}{T_2^*}\right)\left[\frac{1 - \exp\left(-\frac{TR}{T_1}\right)}{1 - \cos\alpha \cdot \exp\left(-\frac{TR}{T_1}\right)}\right]\sin\alpha, \quad [1]$$

where t_p is the phase encoding time, *TR* is the repetition time between successive pulses, ρ is the spin density, and T_1 and T_2^* are the spin–lattice and effective spin–spin relaxation times, respectively. Equation [1] assumes that the transverse magnetization has completely dephased between successive RF pulses, so as to prevent the formation of echoes (*15, 38*), and that the RF pulse bandwidth was sufficient so as to ensure uniform magnetization rotation angles throughout the sample, at all gradient values (*39*).

The two-dimensional SPI pulse sequence is shown in Fig. 1a; the extension to three dimensions can be achieved by the addition of a third phase encode gradient. Images acquired using SPI are free from distortions due to chemical shift, susceptibility variations, and $\mathbf{B}_0$ inhomogeneity (*39*). The use of pure phase-encoding techniques produces images which do not have a linewidth restriction on resolution which is inherent to time-based sampling (frequency encoding) techniques (*39*). We have previously applied this idea to the SPRITE imaging sequence (*15*), as shown in Fig. 1b. The use of the ramped phase gradient in SPRITE allows us to obtain images with greater speed, and with lower overall $d\mathbf{B}/dt$, which minimizes gradient vibration.

[2] Water/cement = 0.5, White Portland cement, 2 mm maximum aggregates (quartz), 3 months moist curing.

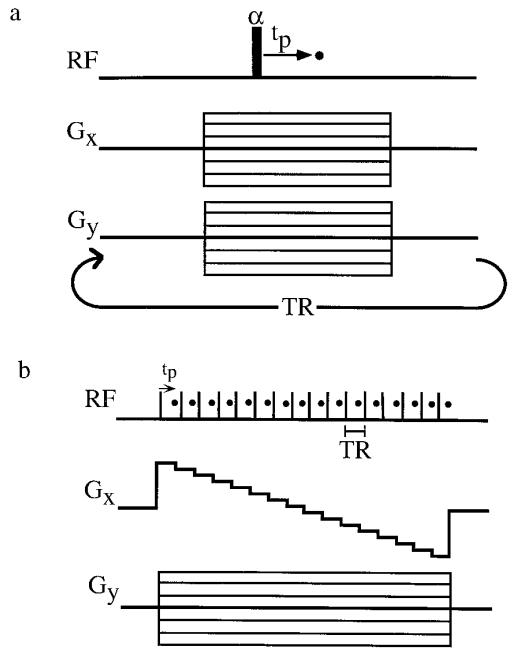

FIG. 1. (a) Single point imaging (SPI) 2D sequence. The image is phase encoded with amplitude cycling of the gradient along the imaging axis. A single point is acquired time t_p after a brief (broadband) low flip angle RF pulse, α, is applied in the presence of the gradient. The encoding time is t_p and the RF pulse repetition time is *TR*. (b) SPRITE 2D imaging sequence. The gradient is stepped with an RF pulse at every gradient amplitude, which leads to imaging times which are decreased by as much as an order of magnitude compared to SPI. We typically employ 64 or 128 steps each of approximately 1–4 ms duration. A second phase-encode gradient is amplitude cycled to encode the second dimension. The encoding time is t_p, and the repetition time, *TR*, is the time between subsequent RF pulses at each gradient step.

NEW RELAXATION TIME MAPPING METHODS

SPRITE T_2^* Mapping

By examining Eq. [1] we can see that by using a long *TR*, and/or a small RF flip angle, α, we obtain an image of spin density, ρ, weighted purely by the local T_2^*,

$$S \propto \rho \exp\left(-\frac{t_p}{T_2^*}\right). \quad [2]$$

Therefore, by acquiring a series of SPI images with variable encoding time, t_p, we could obtain a spatial map of T_2^*, as previously described by Axelson *et al.* (*4*). Here we propose the use of the SPRITE sequence to obtain the T_2^* map. The use of SPRITE instead of traditional SPI methods allows us to either acquire the image faster or, conversely, better define the T_2^* decay curve, through more experimental time points, in the same amount of time as the analogous SPI experiment.

When T_2^* mapping with a variable t_p we must adjust the magnitude of the gradient step size in order to maintain a constant *k*-space step, $\Delta k = (\gamma/2\pi)\Delta G \cdot t_p$ (FOV = $1/\Delta k$).

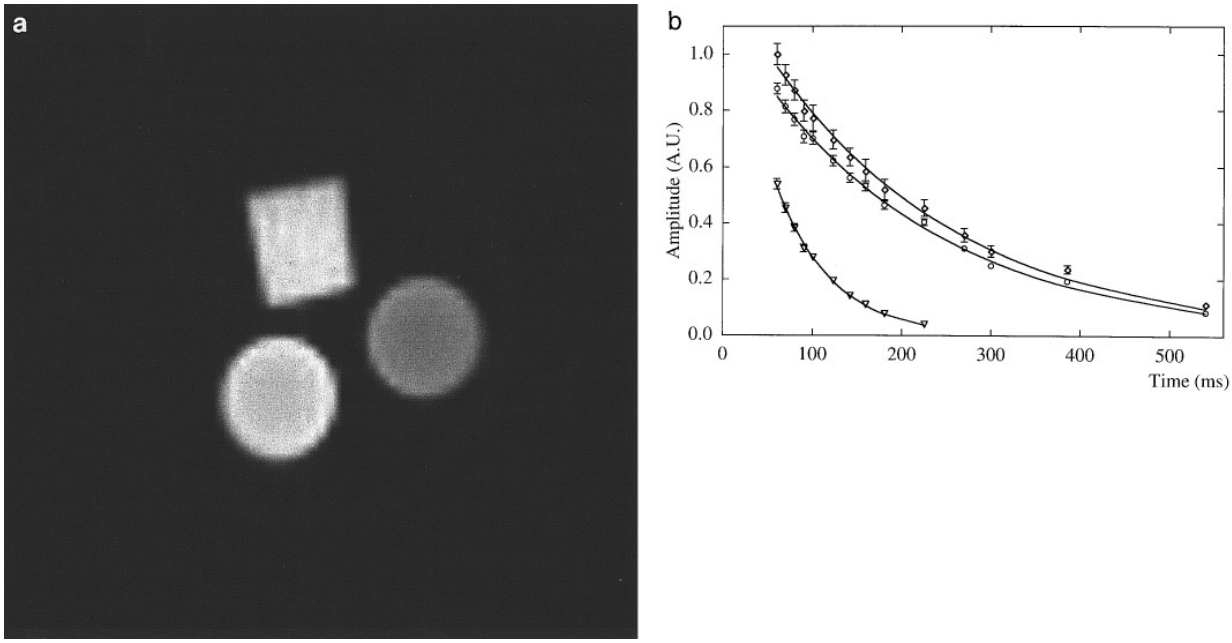

FIG. 2. (a) The 2D SPRITE T_2^*-weighted image, shown here for $t_p = 80$ μs, of two Mn(II)-doped agarose gels, with bulk T_2^*'s of 209 $\pm$ 1 μs (lower left) and 65 $\pm$ 2 μs (lower right), and a cube of White Portland cement mortar (top) (w/c = 0.5, 3 months of curing), with a bulk T_2^* of 218 $\pm$ 1 μs. Images were acquired at 14 different encoding times ranging from 60 to 540 μs, using a RF pulse repetition time, *TR*, of 2 ms and 24° flip angle pulse (α). The bright ring observed in the gel phantoms is due to the meniscus formed by the gel in the glass vial. A small amount of masking tape is visible in the image to the right of the most heavily doped gel phantom. (b) Plots of average image intensity from all three objects in the images (5 $\times$ 5 pixel ROI). The T_2^* values are 206 $\pm$ 5 μs ($\bigcirc$) and 63 $\pm$ 2 μs ($\triangledown$) for the two doped gels and 211 $\pm$ 7 μs ($\diamond$) for the mortar. Error bars are the standard deviation of pixel intensities within the 5 $\times$ 5 pixel ROI. Error bars are largest for the mortar due to the heterogeneity of the material.

In principle it is possible to acquire multiple data points on the free induction decay. Note however that because they will have different encoding times, t_p, images reconstructed from each separately will have varying FOV. Such images will also have a variable T_2^* weighting, Eq. [2], and therefore are appealing for T_2^* mapping. We feel however that a simple pulse sequence with consistent FOV, in the first instance, is preferable.

Using this method we have obtained a two-dimensional T_2^* map of the three phantoms described above. Fourteen images (64 $\times$ 64) were obtained with phase-encoding times ranging from 60 to 540 μs, in a total imaging time of 7 h, with 32 signal averages, using a 24° RF flip angle (8 μs) and SPRITE gradient step length (*TR*) of 1.5 ms. The FOV of the images obtained was 8 $\times$ 8 cm. A sample image from the data set, exhibiting T_2^* contrast, is shown in Fig. 2a. Plots of the average image intensity of a 5 $\times$ 5 pixel region of interest (ROI) within the phantom images versus encoding time are shown in Fig. 2b for each sample. Error bars are the standard deviation of the average pixel intensities within the defined box. It was found throughout the course of these experiments that the largest error was not due to pixel to pixel variations, but rather due to changes in the instrumentation (e.g., probe tuning) during the course of the experiment. Values for T_2^* obtained from the fit image data shown in Fig. 2b were 206 $\pm$ 5 μs, 63 $\pm$ 2 μs, and 211 $\pm$ 7 μs for the two Mn-doped gels and the mortar sample, respectively, which agree very well with the previously stated bulk values.

A second two-dimensional T_2^* mapping experiment was then performed using a poly(ethylene) polymer ($T_{1L} \approx 400$ ms), to demonstrate the ability of this experiment to resolve bi-exponential relaxation components, and to show the mapping method may be employed for samples with short T_2^* but long T_1 (shown in Fig. 3a). The phantom used was a 4-cm-diameter poly(ethylene) cylinder, 8 cm in length, with a 2-cm hole drilled in its centre, into which was inserted another 2-cm-diameter poly(ethylene) cylinder. The inner cylinder of poly(ethylene), otherwise identical to the outer sample, underwent prolonged exposure to light, and was visibly discoloured. In these experiments the rigid crystalline T_2^* component ($\approx$5 μs) is not observed, due to hardware limitations on the shortest possible phase-encoding time. Blümich has shown that physical and chemical aging can lead to changes in relaxation times in polymer materials. These changes are often not very pronounced in the T_1, T_2, and T_2^* time constants (*40*). Our experiments have shown that the samples have $T_{1\rho}$ differences, but they do not appear to have significantly different T_2^* relaxation behaviour. The average bulk values for the two observed components were 18.0 $\pm$ 0.1 μs and 94.9 $\pm$ 0.1 μs, which correspond to the mobile crystalline (or highly immobilized noncrystalline) and amorphous phases, respectively (*4*).

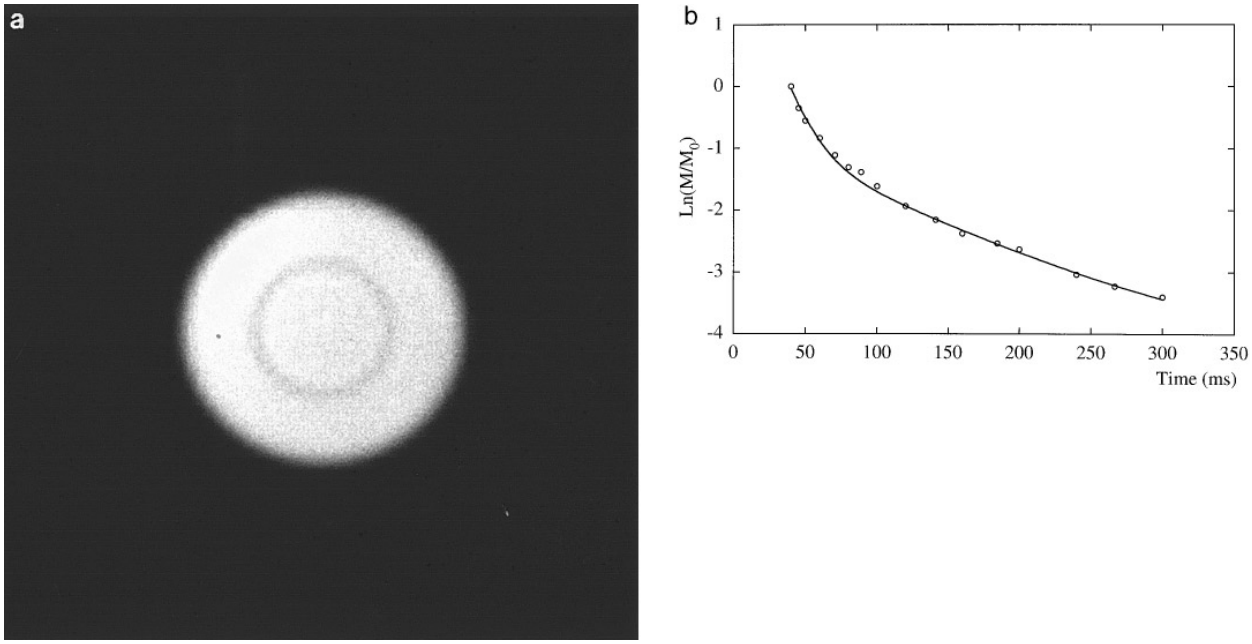

FIG. 3. (a) The 2D SPRITE T_2^*-weighted image, $t_p = 40$ μs, of a 4-cm-diameter poly(ethylene) cylinder, with a 2-cm-diameter hole drilled into its centre, into which was inserted a second poly(ethylene) rod. Images were acquired at 18 different encoding times ranging from 40 to 480 μs, using a TR of 4 ms and 6° flip angle RF pulse. (b) The logarithmic plot of average intensity of a 5 × 5 pixel ROI from an arbitrary position gave two exponentials of 14.0 ± 0.8 μs and 93.8 ± 0.6 μs, which are reasonably close to the bulk values of 18.0 ± 0.1 μs and 94.9 ± 0.1 μs. Although experiments show that there are $T_{1\rho}$ differences, no significant difference in T_2^* behaviour was observed in the two poly(ethylene) phantoms.

The images (64 × 64) were obtained using 18 different phase-encoding times ranging from 40 to 480 μs, and 24 signal averages, using a 6° RF flip angle and SPRITE gradient step length of 4 ms. The FOV of the images obtained was 9.5 × 9.5 cm. The plot of the average image intensity of a 5 × 5 pixel ROI versus encoding time is shown in Fig. 3b. Values for T_2^* obtained from the fit image data for the 5 × 5 pixel ROI were 14 ± 1 μs and 94 ± 1 μs, which agree reasonably well with the values obtained in bulk.

SPI T_1 Mapping

Our proposed T_1 and T_2 mapping techniques employ SPI to obtain the image, with some form of spin preparation imposed before acquiring the SPI *k*-space point. From Eq. [1] we see that for a large flip angle, α, and a *TR* on the order of the T_1, we can introduce T_1 contrast into a SPI image. The measurement is however more sensitive if we introduce a longitudinal recovery, following magnetization inversion, before sampling the SPI point, as shown in Fig. 4. By varying the delay time between the 180° inversion pulse and the sampling pulse, α, we obtain images with local intensity weighted by T_1, as shown in Eq. [3]

$$S \propto \rho \exp\left(-\frac{t_p}{T_2^*}\right)\left[1 - 2\exp\left(-\frac{\tau}{T_1}\right)\right] \qquad [3]$$

assuming the *TR* is long enough so as to allow complete T_1 recovery between sequential RF pulses. Since t_p is a constant, the T_2^* decay is simply a constant weighting term, and the only variation between images is due to T_1 recovery.

The T_1 mapping method was tested in two dimensions using the same three phantoms. A sample image from the data set, this time exhibiting T_1 contrast (the mortar sample has been "nulled"), is shown in Fig. 5a. Plots of average intensity of 5 × 5 pixel ROIs within the three phantom images versus inversion time, τ, are shown in Fig. 5b. When

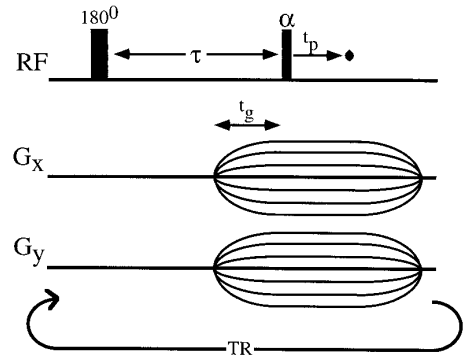

FIG. 4. The 2D SPI T_1-mapping sequence. A 180° inversion pulse is applied before each step of the standard SPI imaging experiment. The shortest delay time between the inversion pulse and the low flip angle sampling pulse, α, is determined by the finite settling time of the switched magnetic field gradients, t_g.

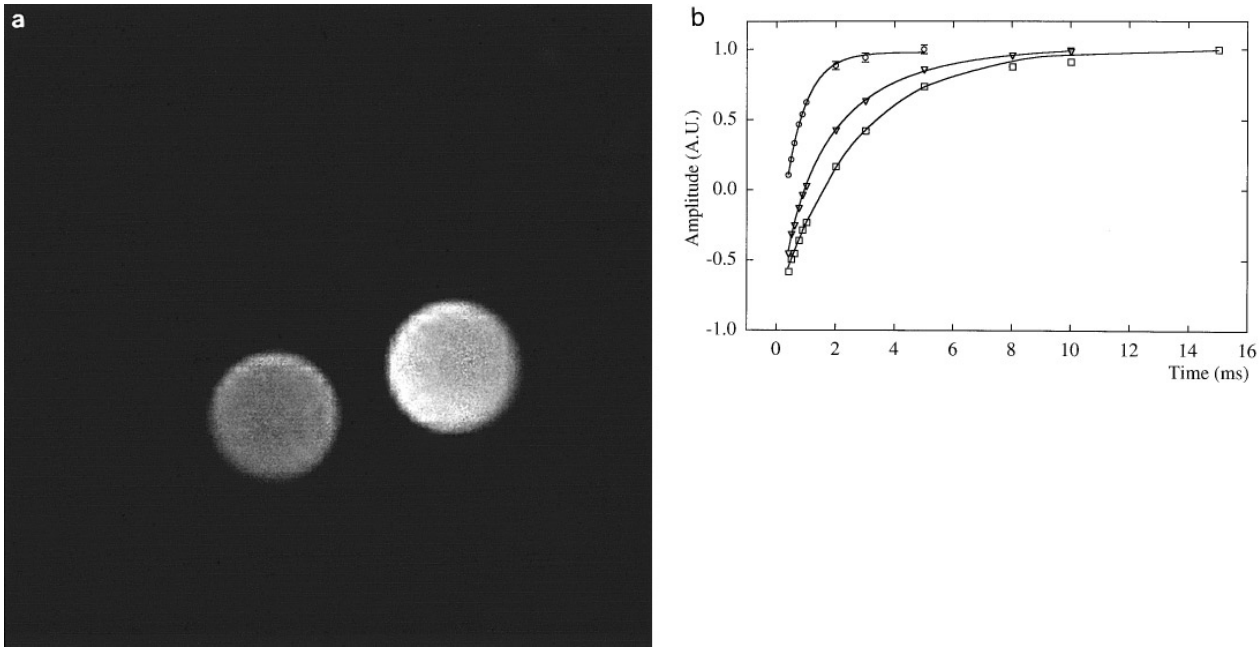

FIG. 5. (a) The 2D SPI T_1-weighted image of two Mn(II)-doped agarose phantoms with T_1's of 2.58 ± 0.01 ms (lower right) and 0.70 ± 0.01 ms (lower left) and a mortar sample with a $\tilde{T}_1$ = 1.28 ± 0.02 ms (α = 0.69 ± 0.05), shown here with an inversion delay, τ, of 850 μs, chosen to null the mortar sample for this displayed image. Images (9 cm × 9 cm) were acquired using 12 inversion delays, τ, ranging from 400 μs to 15 ms, with a t_p = 60 μs, and a RF flip, α, of 24°. (b) Plots of average image intensity from three different points in the images (5 × 5 pixel ROI). T_1 recoveries for the doped gels were fit to single exponentials, giving values of 0.68 ± 0.03 ms (○) and 2.62 ± 0.07 ms (□). The data for the mortar were fit to a stretched exponential recovery, giving 1.32 ± 0.09 ms (α = 0.69 ± 0.05) (▽) for the mortar. These results agree with the bulk values of 0.70 ± 0.01 ms and 2.58 ± 0.01 ms for the gels, and 1.28 ± 0.02 ms (α = 0.64 ± 0.01) for the mortar. Error bars are the standard deviation of pixel intensities within the 5 × 5 pixel ROI.

the data for the doped agarose gels were fit to a single exponential recovery, values of T_1 = 0.68 ± 0.03 ms and T_1 = 2.62 ± 0.07 ms were found, which agree with the bulk values. When the average intensity of a 5 × 5 pixel ROI from the mortar was fit to a stretched exponential, we obtained a value of $\tilde{T}_1$ = 1.32 ± 0.09 ms (α = 0.69 ± 0.05) which agrees with the previously stated bulk values. These values are also comparable to the values obtained by Blinc *et al.* (*22*), and demonstrate the ability of this method to resolve multiexponential T_1 behaviour, even for very short T_1's. As illustrated schematically in Fig. 4, there is a lower limit to the smallest delay value which can be used, due to the finite rise time of the gradient. However, even with T_1's < 1 ms, satisfactory mappings can be obtained with gradient switching times of several hundred microseconds. The mapping (64 × 64) was acquired with 12 inversion times ranging from 0.4 to 15 ms in 7 h, with 8 signal averages, using a 24° RF flip angle, t_p = 60 μs, with a FOV = 9 × 9 cm.

In this experiment we are limited in our minimum repetition rate (TR) by 5 times the longest T_1 we wish to map. Therefore, in order to obtain the mapping in a reasonable amount of time, the longest T_1 which can reasonably be mapped is about 30 ms. We are developing SPRITE-based T_1 mapping methods which are able to study samples with a short T_2^*–long T_1 (such as polymers).

SPI T_2 Mapping: CPMG Method

The method we propose for spatially mapping the spin–spin relaxation time, T_2, requires spin preparation with a CPMG echo train with subsequent acquisition of the SPI point as shown in Fig. 6. We interrupt the echo train after n echoes, z-store the transverse magnetization, then switch the field gradient on and sample the T_2-weighted longitudinal magnetization with a low flip angle pulse. The z-storage is necessary in

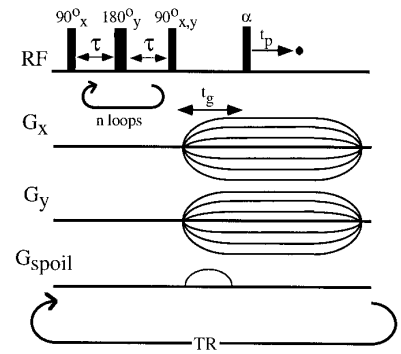

FIG. 6. The 2D SPI T_2-mapping CPMG sequence. The magnetization is z-stored after a variable number, n, of spin echoes, and is then sampled and phase encoded using SPI in the usual way. Magnetization z-stored on the + and − z axes is subtracted to eliminate T_1 effects on the observed decay. A spoiling gradient is needed to prevent the formation of echoes due to imperfect pulses.

order to avoid spin dephasing of the magnetization during the gradient switch (*38*). It has the added advantage that it places the "prepared" magnetization along the axis with the longest relaxation time. We employed a spoiling gradient to prevent the formation of echoes at low amplitude phase-encode steps. Repeating this experiment with a variable number of CPMG echoes produced images whose signal amplitudes decay as a function of T_2. The *z*-storage will however introduce T_1 relaxation into the experiment, which leads to images which are a function of both a T_2 decay and a T_1 recovery.

A resolution to this problem may be achieved by consideration of the Bloch equations with appropriate initial conditions. We consider the magnetization in an arbitrary isochromat, and assume that this magnetization is spatially resolved and visualized through SPI. The transverse magnetization, in our arbitrary isochromat, following a CPMG train of *n* echoes (*38*) is

$$M_{x,y}(2n\tau) = M_0\exp\left(-\frac{2n\tau}{T_2}\right). \quad [4]$$

The echo may be stored on either the positive or negative *z*-axis, depending on the phase of the *z*-storage pulse. Therefore, initially following the *z*-storage pulse the longitudinal magnetization from an arbitrary isochromat is

$$M_z(0) = \pm M_0\exp\left(-\frac{2n\tau}{T_2}\right). \quad [5]$$

However, there is a finite period of time, t_g, due to the settling time of the gradient, which restricts our ability to sample the "prepared" magnetization arbitrarily close to the *z*-storage pulse. During this time longitudinal recovery occurs. Thus, the magnetization at the time of the application of the low flip angle sampling pulse is

$$M_z(t_g) = \pm M_0\exp\left(-\frac{2n\tau}{T_2}\right)\exp\left(-\frac{t_g}{T_1}\right) + M_0\left[1-\exp\left(-\frac{t_g}{T_1}\right)\right]. \quad [6]$$

For gradient settling times on the order of the spin–lattice relaxation time, or longer, we cannot ignore the T_1 effects. If, however, we subtract the SPI-sampled magnetization stored on the negative *z*-axis after a time t_g from the SPI-sampled magnetization stored on the positive *z*-axis in a subsequent experiment, we obtain

$$\begin{aligned} M_{z(+)} - M_{z(-)} &= 2M_0\exp\left(-\frac{t_g}{T_1}\right)\exp\left(-\frac{2n\tau}{T_2}\right) \\ &= A_0\exp\left(-\frac{2n\tau}{T_2}\right), \end{aligned} \quad [7]$$

where $A_0 = 2M_0e^{-t_g/T_1}$ and is simply a constant at each point in the image. Performing the experiment with *z*-storage on the positive *z*-axis, then repeating the experiment with *z*-storage on the negative *z*-axis and subtracting the *k*-space data, we obtain a *k*-space representation of the object weighted by a pure T_2 decay term,

$$S \propto \rho'\exp\left(-\frac{t_p}{T_2^*}\right)\exp\left(-\frac{2n\tau}{T_2}\right), \quad [8]$$

where ρ' is directly proportional to M_0. We could equivalently subtract the Fourier-transformed "real" profiles; however, by subtracting the *k*-space data we avoid the necessity of phasing the data. This method gives accurate T_2 maps; however, the value of M_0, incorporated into A_0, cannot be obtained from the experimental fit. The true M_0 is most reliably obtained in our samples with a T_2^* mapping experiment. We have alternatively fit data obtained using similar methods with one *z*-storage pulse to an offset, to take into account the T_1 recovery term (*19*).

Two-dimensional mappings of the same two doped gels and the mortar were again performed, however, delay times were only optimized for the longer T_2 gel. A sample image from the data set, this time exhibiting pure T_2 contrast, is shown in Fig. 7a. The fit data for the average intensity of a 5×5 pixel ROI within the long T_2 gel image is shown in Fig. 7b. The value obtained from the mapping of $T_2 = 201 \pm 10$ μs agrees with the value obtained from the bulk CPMG measurement. The mapping (64×64) was acquired with 1–6 echoes in 8 h, using 8 signal averages, with a 24° RF flip angle, $t_p = 60$ μs, with a FOV = 9×9 cm. Figure 7c is a stackplot version of one of the negatively *z*-stored 2D SPI T_2-weighted images from the above data set (real component). This plot clearly shows the longitudinal recovery of the short T_1 gel (right, rear) which has recovered significantly during the gradient switching time (t_g) so as to appear as a positive signal in the image, even though the CPMG prepared magnetization was stored on the negative *z*-axis.

SPI T_2 Mapping: Variable TE Method

The CPMG T_2 mapping method suffers from the inherent limitation that the time between successive points in the T_2 decay are time 2τ apart. This means that only a limited number of echoes can be acquired for samples with a very short T_2, which leads to difficulty in accurately fitting the data, especially in samples which exhibit multiexponential behavior. A resolution to this problem is to use the same technique as above, but with a single echo obtained with a variable echo time 2τ. The signal amplitude is then given by Eq. [9],

$$S \propto \rho'\exp\left(-\frac{t_p}{T_2^*}\right)\exp\left(-\frac{2\tau}{T_2}\right). \quad [9]$$

This allows us to acquire T_2-weighted images with near con-

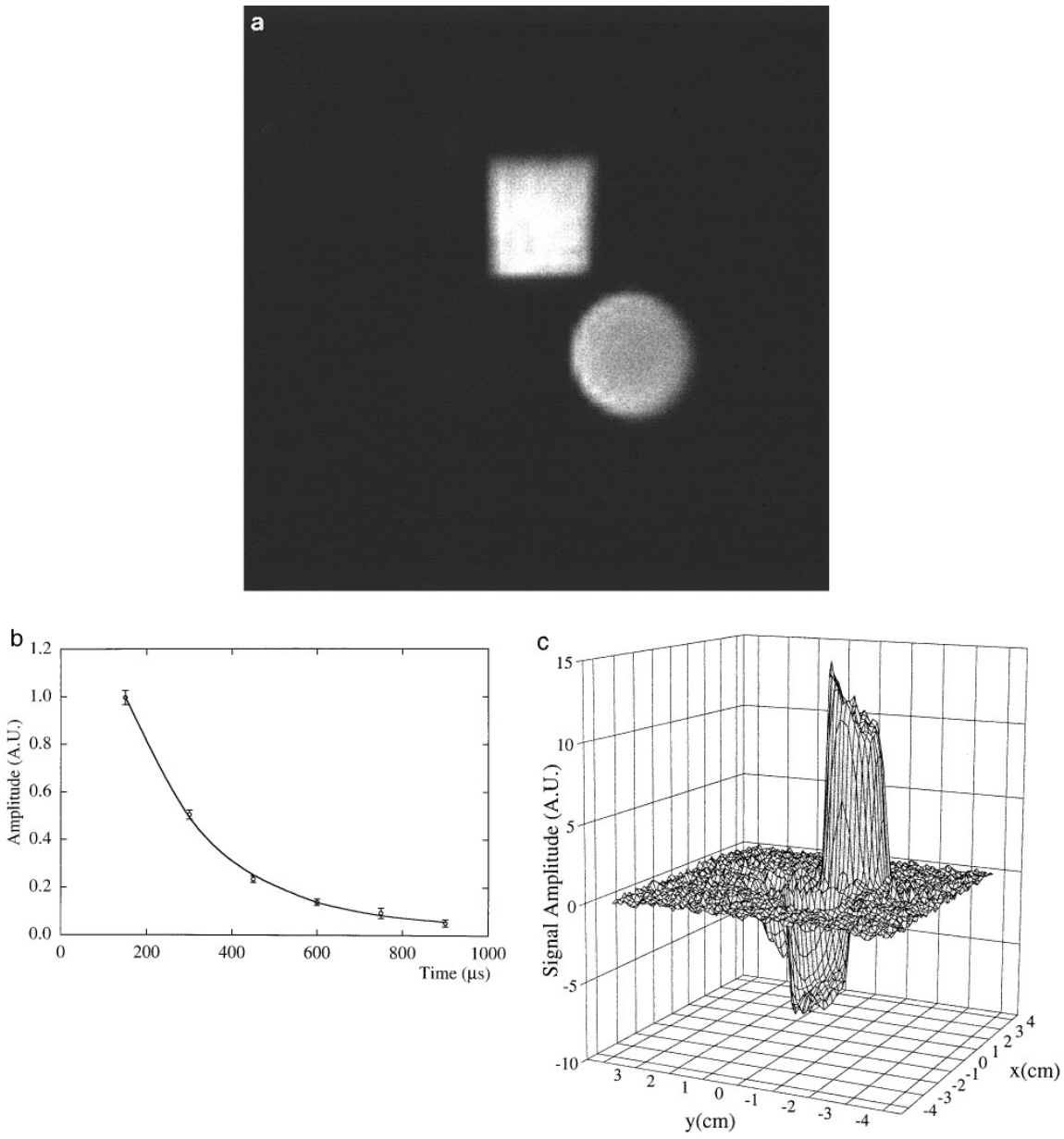

FIG. 7. (a) The 2D SPI T_2-weighted image (CPMG Method) of two Mn(II)-doped gels with bulk T_2's of 210.4 ± 0.4 μs (lower right) and 63 ± 2 μs (lower left) and a mortar sample (top), shown here after the second echo. The Mn(II)-doped agarose phantom with the shortest T_2 is not visible in this image. Images (9 cm × 9 cm) were acquired using 1–6 echoes at an echo time $TE = 150$ μs, using a $t_p = 60$ μs, and a RF flip angle, α, of 24°. Before Fourier transforming, the *k*-space data for magnetization stored on the + and − *z*-axes are subtracted to eliminate T_1 decay effects in the image series. Parameters were chosen to map only the longer T_2 gel. (b) Plots of average image intensity from a 5 × 5 pixel box average for the longer relaxation time Mn(II)-doped gel give a value for T_2 of 201 ± 10 μs (bulk value 210.4 ± 0.4 μs). Error bars are the standard deviation of pixel intensities within the 5 × 5 pixel ROI. (c) Stackplot of the real component of a 2D SPI T_2 weighted image of the two Mn(II)-doped gels and the mortar sample, using only negative *z*-storage (no subtraction). The plot clearly shows the longitudinal recovery of the short T_1 Mn-doped gel (right rear) during the gradient switching time (t_g), which has recovered significantly so as to appear as a "positive" signal in the image, even though all three samples were stored on the negative *z*-axis. The longer T_1 gel (front) and the mortar (partially eclipsed, left rear) have sufficiently long T_1's so as to have remained negative during the gradient switching time. This demonstrates the necessity to subtract images stored on the positive and negative *z*-axes, for samples with spin–lattice relaxation times on the order of the gradient switching time, so as to remove T_1 effects.

tinuous time resolution; however, the measurement suffers from additional spin dephasing due to variable diffusion through sample-based field gradients. We anticipate that in samples where the CPMG and Hahn echo methods produce different results, the difference may potentially be exploited to help determine the underlying sample heterogeneity. However, for samples which are homogeneous, or for solids, this method should provide accurate results even with very short T_2's.

RELAXATION TIME MAPPING OF A HETEROGENEOUS SAMPLE—PARTIALLY DRY CONCRETE CYLINDER

As a practical demonstration of the techniques, we present results of relaxation time mapping of a 50 mm × 70 mm concrete cylinder, containing aggregates graded to a maximum of 14 mm, drying from a single exposed face.[3] Halperin *et al.* (*21*), Blinc *et al.* (*22*), and many others, have studied relaxation parameters in fully saturated cement paste in an attempt to extract the pore size distributions (typically 1 nm–10 μm (*35*)). Concrete, however, is usually not fully saturated, and relaxation parameters therefore vary in a way that depends not only on the underlying pore structure, but also on the degree of drying (*16, 36*). The relaxation times are thus inherently spatially dependent, which renders any bulk measurement less meaningful. Although the pores themselves are significantly smaller than the resolution of an MRI image, important information on pore occupancy may be connected to the mechanism of concrete drying (*16, 36, 37*) through studies of the macroscopic spatial variation of the relaxation times.

At the time of the experiment the sample had been drying at 21 ± 2°C and 40 ± 10% R.H. (*r*elative *h*umidity) for three days, following a moist curing period of seven days. Bulk measures of T_1 and T_2 were both multiexponential (*16, 19, 22*), due to surface relaxation effects in a distribution of pore sizes (*18, 21*), and the T_2 is fit to a two exponential decay while the T_1 is fit to a stretched exponential. The variable echo time T_2 mapping method was used in this case, to ensure sufficient experimental points to determine the local multiexponential decay. Multiexponential T_1 and T_2 behavior is observed at all positions in the experimental profiles (Figs. 8a, 8b). We also observed a clear trend in the T_1 and T_2 relaxation time parameters as we move across the profile, away from the drying front. Trends in both the T_1 and the α parameter (related to surface/volume of the pore structure (*22*)) are shown in Figs. 9a, 9b.

It is important to note that although the observed T_2's are multiexponential, the T_2^* map of the concrete cylinder is single exponential (Fig. 8c). We believe this is due to the inherent heterogeneity of the concrete material and the fact that each pixel in a 1D profile is an average over a large 2D disk and therefore incorporates the dephasing effects of a large distribution of field variations (*22, 41, 42*). This effectively reduces each T_2 component to a single shorter T_2^* value due to the fact that the T_2^* relaxation mechanism is dominated by the inhomogeneous broadening due to random field variations (*42*). This is a valuable result because it allows us to determine accurate ρ maps, based on the value of M_0 determined from the T_2^* fit (*16*). The precision of this M_0 determination has been confirmed by mass measurements of drying concrete specimens (*16*). It is important to note as well, that while T_1 and T_2 vary spatially with drying, T_2^* does not, within error, vary spatially across the one-dimensional profile.

[3] Water/cement = 0.5, White Portland cement, 14 mm maximum aggregate, quartz fine and coarse aggregates, 7 days moist curing.

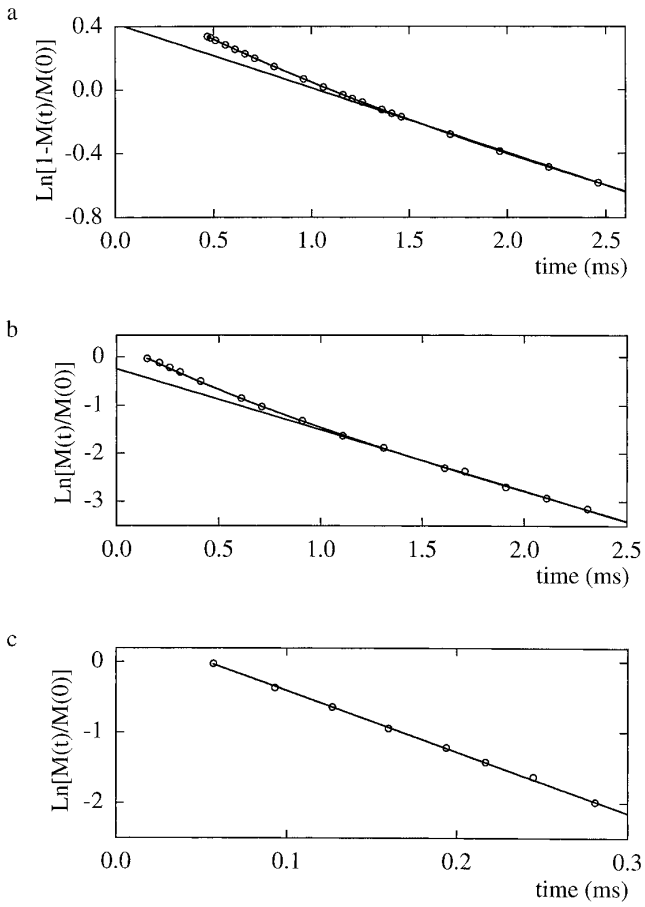

FIG. 8. (a) T_1-mapping data from an arbitrarily chosen position in a partially dry 50-mm-diameter concrete cylinder, exposed from a single face. The data were fit to a stretched exponential, with $\tilde{T}_1 = 1.51$ ms ($\alpha = 0.68$). (b) T_2-mapping data from an arbitrarily chosen position in the concrete cylinder. At least two components are observed: a long component $T_{2L} = 0.85$ ms, indicated by the straight line, and a short component $T_{2S} = 0.34$ ms. The relative proportions of these two components varies with position. (c) T_2^*-mapping data from an arbitrarily chosen position in the concrete cylinder. The data are apparently single exponential with time constant $T_2^* = 115$ μs.

CONCLUSION

The proposed imaging methods produce quantitative images of both uniform phantoms, polymer materials, and inhomogeneous concrete materials, in one and two dimensions. For standard gradient switching times, maps of T_1, T_2, and T_2^* can be obtained, even for very short relaxation times. We note that these methods can also be used to simply introduce contrast if desired, for example, between two spin populations with different T_1's, using a T_1-null method. Studies, using these methods, of spatially resolved relaxation times in polymers, gas in porous media, drying concrete, and freezing/thawing of saturated and partially dried porous materials are currently under-

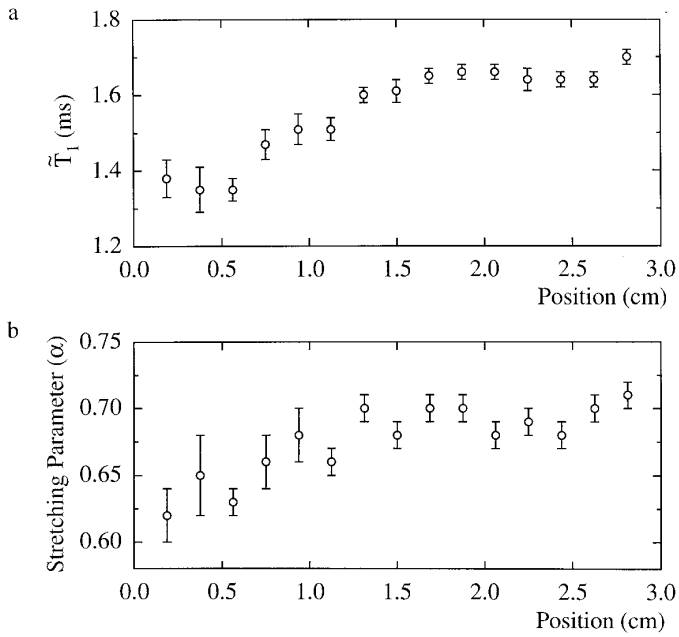

FIG. 9. (a) Variation of $\tilde{T}_1$ with position for a White Portland concrete cylinder (50-mm diameter), which had moist cured for one week, and was then allowed to dry at ambient temperature and humidity, from a single exposed face (Position = 0 cm corresponds to the location of the exposed face). Only points near the exposed face are displayed. (b) Variation of the stretching parameter, α, with position for the same partially dry concrete cylinder. Changes in $\tilde{T}_1$ and α indicate a possible change in relative pore occupancy.

way. Partial *k*-space methods are being developed to decrease image acquisition times.

ACKNOWLEDGMENTS

We thank NSERC of Canada for operating (B.J.B.) and equipment grants (B.J.B., R.L.A.). This work was supported by an NSERC/NRC Research Partnership award (B.J.B., T.W.B., R.L.A.). We also thank Jennifer Perrier and Tom Egan of TecMag, Inc., for useful discussions, and Rod MacGregor for construction of the RF probe and assistance with measurements. We thank Don Hornibrook and Jim Merrill for the fabrication of imaging phantoms.

REFERENCES

1. P. Jezzard, J. J. Attard, T. A. Carpenter, and L. D. Hall, *J. Prog. Nucl. Magn. Reson. Spectrosc.* **23,** 1 (1991).
2. P. Kinchesh, E. W. Randall, and K. Zick, *J. Magn. Reson.* **100,** 411 (1992).
3. P. J. McDonald, *Meas. Sci. Technol.* **4,** 896 (1993).
4. D. E. Axelson, A. Kantzas, and T. Eads, *Can. J. Appl. Spectrosc.* **40,** 16 (1995).
5. K. Hayashi, K. Kawashima, K. Kose, and T. Inouye, *J. Phys. D* **21,** 1037 (1988).
6. S. Davies and K. J. Packer, *J. Appl. Phys.* **67,** 3163 (1990).
7. P. Mansfield and B. Issa, *J. Magn. Reson. A* **122,** 137 (1996).
8. M. Bogdan, B. J. Balcom, T. W. Bremner, and R. L. Armstrong, *J. Magn. Reson. A* **116,** 266 (1995).
9. G. Papavassiliou, F. Milia, M. Fardis, R. Rumm, E. Laganas, O. Jarh, A. Sepe, R. Blinc, and M. Pintar, *J. Am. Ceram. Soc.* **76,** 2109 (1993).
10. J. Link, J. Kauffman, and K. Schenker, *Magn. Reson. Imaging* **12,** 169 (1994).
11. S. Emid and J. H. N. Creyghton, *Physica B* **128,** 81 (1985).
12. P. J. MacDonald, J. J. Attard, and D. J. Taylor, *J. Magn. Reson.* **72,** 224 (1987).
13. P. Bendel, M. Davis, E. Berman, and G. W. Kabalka, *J. Magn. Reson.* **88,** 369 (1990).
14. Z. H. Cho and Y. M. Ro, *Magn. Reson. Med.* **32,** 258 (1994).
15. B. J. Balcom, R. P. MacGregor, S. D. Beyea, D. P. Green, R. L. Armstrong, and T. W. Bremner, *J. Magn. Reson. A* **123,** 131 (1996).
16. S. D. Beyea, B. J. Balcom, P. J. Prado, D. P. Green, T. W. Bremner, and R. L. Armstrong, *Cem. Conc. Res.* **28,** 453 (1998).
17. P. J. Prado, B. J. Balcom, S. D. Beyea, R. L. Armstrong, and T. W. Bremner, *Solid State NMR* **10,** 1 (1997).
18. P. J. Prado, B. J. Balcom, S. D. Beyea, T. W. Bremner, R. L. Armstrong, and P. E. Grattan-Bellew, *Cem. Conc. Res.* **28,** 261 (1998).
19. P. J. Prado, B. J. Balcom, S. D. Beyea, T. W. Bremner, R. L. Armstrong, R. Pishe, and P. E. Grattan Bellew, *J. Phys. D* **31,** 2040 (1998).
20. *Magn. Reson. Imaging* **14** (7/8), (1996).
21. W. P. Halperin, J.-Y. Jehng, and Y.-Q. Song, *Magn. Reson. Imaging* **12,** 169 (1994).
22. R. Blinc, J. Dolinsek, G. Lahajnar, A. Sepe, I. Zupancic, S. Kumer, F. Milia, and M. M. Pintar, *Z. Naturforsch. A* **43,** 1026 (1988).
23. S. J. Doran, J. J. Attard, T. P. L. Roberts, T. A. Carpenter, and L. D. Hall, *J. Magn. Reson.* **100,** 101 (1992).
24. J. J. Attard, S. J. Doran, N. J. Herrod, T. A. Carpenter, and L. D. Hall, *J. Magn. Reson.* **96,** 514 (1992).
25. C. J. G. Bakker, and J. Vriend, *Phys. Med. Biol.* **29,** 509 (1984).
26. J. Liu, A. O. K. Nieminen, and J. L. Koenig, *J. Magn. Reson.* **85,** 95 (1989).
27. S. P. Cottrell, M. R. Halse, and J. H. Strange, *Meas. Sci. Technol.* **1,** 624 (1990).
28. J. J. Attard, P. J. McDonald, S. P. Roberts, and T. Taylor, *Magn. Reson. Imaging* **12,** 355 (1994).
29. T. B. Benson and P. J. McDonald, *J. Magn. Reson. B* **109,** 314 (1995).
30. P. J. McDonald, *Prog. NMR Spectrosc.* **30,** 69 (1997).
31. P. J. McDonald, *Magn. Reson. Imaging* **14,** 807 (1996).
32. A. D. Bain and E. W. Randall, *J. Magn. Reson. A* **123,** 49 (1996).
33. S. Choi, X.-W. Tang, and D. G. Cory, *Int. J. Imaging Syst. Technol.* **8,** 263 (1997).
34. W. H. Press, B. P. Flannery, S. A. Teukolsky, and W. T. Vetterling, "Numerical Recipes," Cambridge Univ. Press, New York (1986).
35. P. K. Mehta, "Concrete Structure, Properties, and Materials," Prentice Hall, Englewood Cliffs, NJ (1986).
36. J. Selih and T. W. Bremner, *Materials Structures* **29,** 401 (1996).
37. J. Kaufmann and W. Studer, *Materials Structures* **28,** 115 (1995).
38. P. T. Callaghan, "Principles of Nuclear Magnetic Resonance Microscopy," Chap. 2, Clarendon, Oxford (1993).
39. S. Gravina and D. G. Cory, *J. Magn. Reson. B* **104,** 53 (1994).
40. B. Blümich, *Concepts Magn. Reson.* **10,** 19 (1998).
41. G. C. Borgia, R. J. S. Brown, and P. Fantazzini, *Magn. Reson. Imaging* **14,** 731 (1996).
42. A. M. Stoneham, *Rev. Mod. Phys.* **41**(1), 82 (1969).